Review of Alternative Methods for Estimating Terrestrial Emittance and Geothermal Heat Flux for Yellowstone National Park Using Landsat Imagery

Shannon L. Savage and Rick L. Lawrence[1]
Department of Land Resources and Environmental Sciences,
Montana State University, Bozeman, Montana 59717

Stephan G. Custer
Department of Earth Sciences,
Montana State University, Bozeman, Montana 59717

Jeffrey T. Jewett and Scott L. Powell
Department of Land Resources and Environmental Sciences,
Montana State University, Bozeman, Montana 59717

Joseph A. Shaw
Department of Electrical and Computer Engineering,
Montana State University, Bozeman, Montana 59717

Abstract: Yellowstone National Park (YNP) is legally mandated to monitor geothermal features for their future preservation, and remote sensing is a component of the current monitoring plan. Landsat imagery was explored as a tool for mapping terrestrial emittance and geothermal heat flux for this purpose. Several methods were compared to estimate terrestrial emittance and geothermal heat flux (GHF) using images from 2007 (Landsat Thematic Mapper) and 2002 (Landsat Thematic Mapper Plus). Accurate estimations were reasonable when compared to previously established values and known patterns but were likely limited due to inherent properties of Landsat data, the effects of solar radiation, and variation among geothermal areas. Landsat data can be valuable for calculation of GHF in YNP. The method suggested in this paper is not highly parameterized. Landsat data provide the means to calculate GHF for all of YNP and have the potential to enable scientists to identify locations for in-depth study.

INTRODUCTION

Yellowstone National Park (YNP), located in Wyoming, Montana, and Idaho, became the world's first national park primarily because of its geothermal features.

[1]Corresponding author; email: rickl@montana.edu

The land was set aside for the "benefit and enjoyment of the people" and to "provide for the preservation from injury or spoliation of all timber, mineral deposits, natural curiosities, or wonders within said park, and their retention in their natural condition" (Yellowstone Park Act, 16 U.S.C. 21 et seq., 1872). Currently there are recognized threats to the geothermal features of YNP, including potential geothermal development in Idaho and Montana, and oil, gas, and groundwater development in Wyoming, Montana, and Idaho (Sorey, 1991; Custer et al., 1993; Heasler et al., 2004). As a result, the National Park Service (NPS) is legally mandated to monitor and protect geothermal features within its units, and YNP in and of itself is listed as a significant geothermal feature (Geothermal Steam Act, 30 U.S.C. 1001-1027, 1970 as amended in 1988).

Geothermal heat flux (GHF), measured in watts per meter squared (Wm^{-2}), is the heat change in water and steam in geothermal systems and is radiated, or emitted, from the surface of the Earth. It represents only heat coming from below the surface and does not include any accumulated indirect or direct solar heating effects. Indirect effects include convection from air currents and conduction of solar energy in soil, and direct effects include solar heating due to variations in topography such as on south-facing slopes. GHF can be measured directly from bore holes via thermocouples (Sorey, 1991), by estimation from other indirect measurements such as chloride flux (Fournier et al., 1975; Norton and Friedman, 1985; Friedman and Norton, 2007), or by utilizing remote digital thermal sensors (Boomer et al., 2002). Terrestrial emittance represents the heat emitted from the ground and is composed of GHF and includes direct and indirect solar radiation effects.

Chloride flux has been used as a proxy to determine GHF in YNP (Fournier et al., 1975; Norton and Friedman, 1985; Friedman and Norton, 2007). Measurements of the rate of flow and chloride content of rivers draining hot spring areas have been made at U.S. Geological Survey (USGS) gauging stations located throughout YNP since 1966. These measurements were used to calculate heat flow in various regions of YNP. The GHF of YNP has been estimated to be 1,800 mWm^{-2}, 30 times the continental average (Fournier et al., 1975; Smith and Siegel, 2000; Waite and Smith, 2002).

More recently, on October 9, 2002, two sets of airborne multispectral imagery were acquired over the Norris Geyser Basin area (one flight near solar noon and the other at night) (Hardy, 2005; Seielstad and Queen, 2009). These data were collected to identify, classify, and map geothermal features. Five spectral bands were acquired and utilized in the image processing: one thermal infrared (TIR), one near infrared (NIR), and three from the visible portion of the electromagnetic spectrum (EMS). The methods developed demonstrated that a geothermal gradient could be classified, mapped, and defined using high-spatial-resolution airborne thermal imagery. These methods, while useful for a very small area, are currently impractical to apply to the entirety of YNP due to time and cost constraints.

Multispectral Landsat satellite imagery has been used to map geothermal heat and activity in a variety of situations. Landsat Thematic Mapper (TM) and Enhanced Thematic Mapper Plus (ETM+) imagery, for example, have been used successfully to map and analyze volcanic features (Andres and Rose, 1995; Kaneko and Wooster, 1999; Flynn et al., 2001; Urai, 2002; Patrick et al., 2004). Other examples include studies that have used TM and ETM+ data to map lineaments (e.g., fault lines) as part of the process of finding geothermal areas (Bourgeois et al., 2000; Song et al., 2005)

and to map minerals such as iron oxide and hydrothermally altered soil (Carranza and Hale, 2002; Daneshfar et al., 2006; Dogan, 2008).

Landsat thermal imagery, however, has rarely been used to assess the spatial distribution of GHF in YNP (but see Watson et al., 2008). The method developed by Watson et al. (2008) to quantify the intensity of surficial geothermal activity at YNP was developed with 2000 Landsat ETM+ imagery, and the results suggested good potential for geothermal monitoring. Thermal radiance data from ETM+ imagery were utilized to estimate terrestrial emittance. Estimates of nongeothermal-related heat were incorporated with terrestrial emittance to subsequently measure and create a map of continuous variations in residual terrestrial emittance (i.e., no solar effects) that was hypothesized to represent the lowest possible values of GHF in each pixel.

The Watson et al. (2008) method utilized a spectral library of "light yellowish brown loamy sand" from the NASA Jet Propulsion Laboratory (JPL) to estimate a single emissivity value for the entire image. This method might be improved upon by assigning emissivity on a pixel-by-pixel basis rather than using a single value. Emissivity can be estimated from the Normalized Difference Vegetation Index (NDVI) that uses the red and near infrared (NIR) Landsat bands to characterize healthy green vegetation (Brunsell and Gillies, 2002). The estimated emissivity can then be applied to the calculation of terrestrial emittance, and thus to estimates of GHF. Incorporating emissivity on a per pixel basis rather than as one value across the entire image potentially increases the precision of the GHF calculations.

Using Landsat data to estimate GHF presents many challenges. Solar radiation and related topographic effects have substantial impacts on total emittance calculations since, for example, south-facing slopes that have no GHF will often have high terrestrial emittance values (Watson, 1975; Kohl, 1999; Gruber et al., 2004). The effect of surface albedo is also an important component and problematic in the calculation of GHF, because dark areas such as large parking lots (e.g., in the Old Faithful area) or recently burned areas absorb and re-emit larger amounts of solar radiation than bright surfaces, resulting in high terrestrial emittance readings that might not include a GHF component (Watson, 1975; Coolbaugh et al., 2007).

Another set of challenges of using Landsat data to estimate GHF stems from the inherent characteristics of the Landsat sensors. The Landsat ETM+ sensor is superior to the Landsat TM sensor because its thermal sensor is kept calibrated by a more stable radiative cooler and it has finer spatial resolution (NASA, 2009). There are only four years of complete data available from Landsat ETM+, while Landsat TM is 25 years old and its thermal sensor, which had a design life of 5 years, has deteriorated over the years, as evidenced by the calibration offset error that was corrected in 2007 (Barsi et al., 2007). This deterioration might also make changes in GHF more difficult to detect. The pixel resolution for both ETM+ (60 m) and TM (120 m) thermal data is much coarser than for the reflective data from both sensors (30 m). When one pixel is 60 × 60 m (3,600 m²) or 120 × 120 m (14,400 m²), effects from small geothermal features or areas are averaged over the pixel. Also, due to the large pixel size it is impractical to accurately calibrate to ground temperatures collected at a single point and impossible to do with historical Landsat imagery.

Our primary objective was to evaluate the utility of Landsat TM and ETM+ thermal data for monitoring GHF. An effective method would enable the accurate measurement of terrestrial emittance and GHF covering the entirety of YNP that
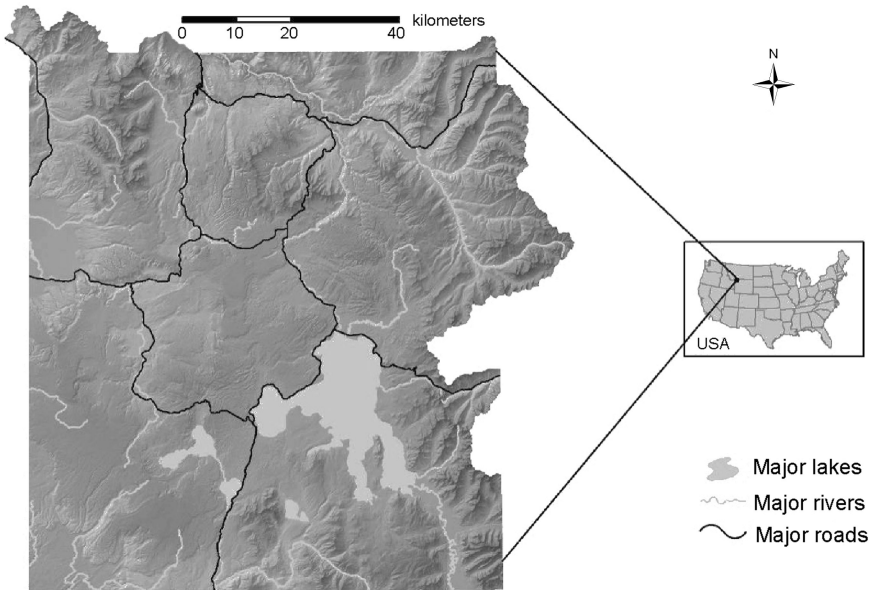
Fig. 1. Location map for Yellowstone National Park displayed with a shaded relief background.

could then be applied to additional Landsat images for use in monitoring and change analyses.

METHODS

Study Area

YNP encompasses approximately 890,000 ha (Fig. 1). Elevation ranges from 1,567 m to 3,458 m (Spatial Analysis Center, 1998). Vegetation includes grassland, shrubland, and forest, with bare ground interspersed. Average precipitation is 25–30 cm in the lower elevations and up to 203 cm in the higher elevations (Spatial Analysis Center, 2000), with warm, dry summers and cold, wet winters (Western Regional Climate Center, 2005). The currently defined geothermal areas (defined by staff at YNP and based on locations of geothermal features and geothermally influenced ground) (Spatial Analysis Center, 2005) comprise less than 1% of the entire area of YNP with the majority concentrated within the 640,000-year-old caldera boundary.

Data Acquisition

YNP is centered within Landsat Path 38 Row 29. A TM scene from June 25, 2007 was acquired from the USGS Earth Resources Observation and Science (EROS) Data Center and an ETM+ scene from July 5, 2002 was acquired from MontanaView (2008).

TM and ETM+ sensors collect data in seven spectral bands, one of which is in the TIR portion of the EMS (10.4 to 12.5 μm). The TM instrument collects TIR data in 120 m pixels, whereas the ETM+ instrument collects TIR in 60 m pixels. Both TM and ETM+ TIR data are provided as 60 m pixels from the EROS Data Center. Both instruments collect the remaining six spectral bands in 28.5 m pixels (resampled to 30×30 m or 900 m^2, by EROS Data Center).

Image Preprocessing

Each image was clipped to the YNP boundary. Clouds and cloud shadows were masked by on-screen digitizing. Elevations greater than 2,700 m were masked to remove snow from the input data. The COSine Transformation (COST) (Chavez, 1996) method of dark-object-subtraction atmospheric and radiometric correction was applied to the original raw data values of the six reflective bands of each image. The original Landsat raw data values are represented by digital numbers (or DNs) with values from 0 to 255 (8-bit radiometric resolution). The dark-object DN values were chosen by examining the image histogram for each of the six reflective bands. The DN value where the histogram increased to more than 100 pixels was assigned the dark-object value. These values along with published calibration factors (Chander et al., 2009) and information from the Landsat header files were used to convert the images to surface reflectance values for Landsat bands 1, 2, 3, 4, 5, and 7 at a 30 m pixel size (Utah State University, 2008).

NDVI was used to estimate fractional vegetation (Fr, unitless) based on the method by Brunsell and Gillies (2002). Fractional vegetation represents the percentage of vegetation within a pixel and is derived from NDVI as follows:

$$Fr = [(NDVI - NDVI_0)/(NDVI_{max} - NDVI_0)]^2 , \qquad (1)$$

where $NDVI_0$ and $NDVI_{max}$ represent scene-specific single values of bare soil and maximum vegetation, respectively. Assuming average broad-band emissivity for bare soil of 0.97 (from the "light yellowish brown loamy sand" and "white gypsum dune sand" JPL spectral libraries [NASA, 2008]) and emissivity for vegetation of 0.98 (from the "coniferous vegetation" JPL spectral library [NASA, 2008]), emissivity (ε, unitless) per pixel (excepting water pixels) was estimated from the Fr:

$$\varepsilon = Fr*\varepsilon_v + (1 - Fr)*\varepsilon_s , \qquad (2)$$

where ε_v represents vegetation emissivity and ε_s represents soil emissivity. Water pixels were assigned an average broad-band emissivity value of 0.99 (Shaw and Marston, 2000). To match the lower-resolution TIR imagery, the resulting emissivity image was subsequently degraded to 60 m and 120 m pixels by averaging the 30 m pixel values.

Potential annual direct incident solar radiation (SR) was calculated from a 30 m digital elevation model (DEM) of the study area (McCune and Keon, 2002) to take solar effects into account. This equation incorporated the slope, aspect, and latitude of the terrain and returns SR in units of MJ cm^{-2} yr^{-1}:

$$SR = 0.339 + 0.808(\cos(L)*\cos(S)) - 0.196(\sin(L)*\sin(S)) -$$
$$0.482(\cos(A)*\sin(S)) , \tag{3}$$

where L = latitude in radians, S = slope in radians, and A = folded aspect in radians east of north.[2] The output values were multiplied by 316.89 Js^{-1}m^{-2} to arrive at SR in Wm^{-2}. This image was degraded to 60 m and 120 m pixel images.

Albedo was calculated from five of the six reflective Landsat bands (Liang, 2000). The green band (band 2) was excluded because it does not improve the R^2 of the regression test presented in Liang (2000). The surface reflectance values calculated from the DNs were applied to the following shortwave albedo calculation (unitless):

$$\alpha_{short} = 0.356\alpha_1 + 0.130\ \alpha_3 + 0.373\ \alpha_4 + 0.085\ \alpha_5 + 0.072\ \alpha_7 - 0.0018 , \tag{4}$$

where $\alpha_\#$ refers to the Landsat band (Liang, 2000).

GHF Calculation Procedures

The raw TIR data (band 6) for each image were converted to at-satellite radiance (L_λ, Wm^{-2}sr^{-1}µm^{-1}) using published calibration factors (Chander et al., 2009). Radiance was converted to top-of-atmosphere emittance (M_{toa}, Wm^{-2}) by integrating over the bandwidth (from 10.4 µm to 12.5 µm = 2.1 µm) and the projected solid angle of the hemisphere (π sr):

$$M_{toa,\ 6H} = 2.1\pi L_\lambda . \tag{5}$$

MODerate resolution atmospheric TRANsmission (ModTran) was utilized to estimate atmospheric transmittance (τ) and upwelling atmospheric emittance (M_{up}, Wm^{-2}) for a "Mid-Latitude Summer" model atmosphere (Ontar Corporation, 2001). Following the Watson method (Watson et al., 2008), surface emittance integrated over band 6 ($M_{surf,\ 6H}$, Wm^{-2}) was estimated:

$$M_{surf,6H} = (M_{toa,6H} - M_{up})/\tau , \tag{6}$$

where M_{up} = 4.64 Wm^{-2} and τ = 89.39%. The fitted coefficients from Watson's regression model were utilized to estimate broad-band surface emittance (M_{surf}, Wm^{-2}):

$$M_{surf} = (0.004812 M_{surf,6H})^2 + 2.653 M_{surf,6H} + 181.8 . \tag{7}$$

Terrestrial emittance (M_{terr}, Wm^{-2}) was estimated using the NDVI-derived emissivity values and downwelling atmospheric emittance (M_{down}, Wm^{-2}) calculated with ModTran for a "Mid-Latitude Summer" model atmosphere:

---

[2]This rescales 0–360° to 0–180°, so NE = NW, E = W, and so on, so that north/south contrasts would be emphasized, a critical issue in the Yellowstone ecosystem (Parmenter et al., 2003).

$$M_{terr} = M_{surf} - (1 - \varepsilon)M_{down} \,, \tag{8}$$

where ε ranges from 0.97 to 0.99, and $M_{down} = 240$ Wm^{-2}.

Estimates of GHF were calculated in three different ways. The first estimate utilized the mean M_{terr} value for non-geothermal ground within YNP for each date (mean $M_{terr,NG}$) based on the defined geothermal area boundaries. By subtracting the mean non-geothermal value, the resulting positive values should on average represent geothermal heat:

$$GHF_M = M_{terr} - \text{mean } M_{terr,NG} \,. \tag{9}$$

Based on the assumption that solar radiation directly and indirectly heats the ground and can be confused with geothermal heat emitted from the ground, a second estimate of GHF was calculated for each image to account for solar effects:

$$GHF_{SR} = M_{terr} - SR \,. \tag{10}$$

A third estimate of GHF was calculated by incorporating albedo into Equation (8) so that locations with low albedo and high absorption of solar radiation, for instance a recent fire scar, would not result in falsely high GHF:

$$GHF_\alpha = M_{terr} - (SR * (1 - \alpha_{short})) \,, \tag{11}$$

where $1 - \alpha_{short}$ is absorption based on Kirchoff's law (Elachi, 1987).

Field validation of these equations was not conducted because precise field measurement of GHF would require multiple samples at each test site and an extensive number of test sites throughout the study area (increasing costs by tens of thousands of dollars), many of which have limited access because of safety and resource protection issues. Field validation would have provided a statistical assessment of the accuracy of these data. The results of the equations, however, could be evaluated in several ways for reasonableness. First, summary statistics of the four methods—M_{terr}, GHF_M, GHF_{SR}, and GHF_α—were calculated for each date. Values of all pixels within the defined geothermal areas were compared to the 57-year average annual air temperature of YNP (4.64° C, or 337.6 Wm^{-2}) (Western Regional Climate Center, 2005) to ascertain which method had the most pixels above that average. Second, the 2002 image was subtracted from the 2007 image for each method so the range of change between years could be observed. The differenced images were also visually inspected to determine the extent to which each method accounted for solar effects. Third, the hottest 10% and coolest 10% of the pixels within YNP were calculated, mapped, and visually evaluated for spatial patterns. These hottest and coolest pixels were also clipped to the defined geothermal areas in order to evaluate which method contained the most of the hottest pixels and the least of the coolest pixels within areas that are expected to be mostly hot. Fourth, the number of the top 10% hottest pixels in which points from the Thermal Inventory Project fell was tabulated for two of the four methods (M_{terr} and GHF_α) to find which method corresponded most to geothermal feature

locations.[3] Fifth, the mean value of three of the four methods (M_{terr}, GHF_{SR}, and GHF_{α}) was calculated for all areas within YNP but outside the defined geothermal areas and again for only pixels within the defined geothermal areas. The differences between the means of the defined geothermal area pixels and those outside the defined geothermal areas were calculated and compared among methods to determine which showed the largest difference and thus had more hot pixels within the defined geothermal areas.

Comparison with Airborne Data

The M_{terr} values for the July 2002 image in the Norris Geyser Basin area were compared to the summary statistics and heat flow values from a nighttime airborne thermal image of the same area from October 2002 (Hardy, 2005; Seielstad and Queen, 2009). The Hardy (2005) data originally had a spatial resolution of 0.76 × 0.76 m. These pixels were degraded to 60 × 60 to match the Landsat data. Two extents were examined: (1) the entire extent of the Hardy data, and (2) the boundary of Norris Geyser Basin according to the defined geothermal areas (Spatial Analysis Center, 2005). Summary statistics and total heat flow were calculated for the four images and compared.

RESULTS

GHF in YNP

The 2002 ETM+ mean M_{terr} value for non-geothermal areas in YNP was 368.7 Wm^{-2}, while the 2007 TM mean M_{terr} value for non-geothermal areas in YNP was 353.0 Wm^{-2}. SR values in YNP ranged from 0.0 to 363.0 Wm^{-2} with a mean of 275.0 Wm^{-2}. Albedo values for YNP in 2002 ranged from 0.0 to 0.6 and from 0.0 to 0.5 in 2007.

The calculated maximum and mean values for the four methods were higher in 2002 than 2007 for all but GHF_M (Tables 1 and 2). The calculated minimum values were all higher in 2002. The M_{terr}, GHF_{SR}, and GHF_{α} mean values in 2002 were approximately 13–16 Wm^{-2} greater than in 2007. The GHF_M values in 2007, on the other hand, were slightly higher than the 2002 values (approximately 1.0 Wm^{-2}). The 2002 M_{terr} values were the hottest overall, while the 2002 GHF_M values were the coolest overall. The widest range of values was observed in the 2002 GHF_{α} at 363.2 Wm^{-2}, with the next widest range in the 2002 GHF_{SR} at 352.1 Wm^{-2}.

The calculated M_{terr} values were up to three times higher than the values of the GHF models (Tables 1 and 2). The majority of M_{terr} values (median values of 364.7 Wm^{-2} in 2002 and 351.9 Wm^{-2} in 2007) were higher than the average annual air temperature in YNP of 4.64° C (337.6 Wm^{-2}) (Western Regional Climate Center, 2005), while all pixel values calculated with the GHF_M, GHF_{SR}, and GHF_{α} were lower than the average annual air temperature. The GHF_M values were largely below zero with the lowest maximum values of the four methods. The values for GHF_{α} were higher than the GHF_{SR} values for all but the maximum values in 2007.

---

[3]The Thermal Inventory Project is a multi-year National Park Service–sponsored project with the goal of collecting a precise GPS measurement of every geothermal feature in YNP, with over 12,000 points collected thus far.

Table 1. Summary Statistics[a] for for Yellowstone National Park on July 5, 2002 (Wm^{-2})

Equation	Min	Max	Mean	Median	Mode	Std. Dev.
(2.8) M_{terr}	305.8	446.7	366.7	364.7	352.7	17.8
(2.9) GHF_M	−63.0	78.0	−2.1	−4.0	−16.0	17.8
(2.10) GHF_{SR}	5.9	358.0	90.4	84.3	77.4	32.5
(2.11) GHF_α	14.8	378.0	121.0	118.0	111.3	32.4

[a]Summary statistics: terrestrial emittance = M_{terr}; mean non-geothermal value corrected geothermal heat flux = GHF_M; potential annual direct incident solar radiation corrected geothermal heat flux = GHF_{SR}; and albedo and potential annual direct incident solar radiation corrected geothermal heat flux = GHF_α.

Table 2. Summary Statistics[a] for for Yellowstone National Park on June 25, 2002 (Wm^{-2})

Equation	Min	Max	Mean	Median	Mode	Std. Dev.
(2.8) M_{terr}	303.8	433.4	353.1	351.9	353.4	14.8
(2.9) GHF_M	−49.9	79.6	−0.7	−1.9	−0.3	14.8
(2.10) GHF_{SR}	4.6	351.0	76.8	70.9	65.5	31.5
(2.11) GHF_α	14.1	350.7	105.6	102.2	103.5	31.1

[a]Summary statistics: terrestrial emittance = M_{terr}; mean non-geothermal value corrected geothermal heat flux = GHF_M; potential annual direct incident solar radiation corrected geothermal heat flux = GHF_{SR}; and albedo and potential annual direct incident solar radiation corrected geothermal heat flux = GHF_α.

The mean difference between 2002 and 2007 GHF_M values was 0.0 Wm^{-2}, whereas the mean difference between 2002 and 2007 M_{terr}, GHF_{SR}, and GHF_α values were near −15.0 Wm^{-2} (Table 3). The maximum value of the difference in M_{terr} was less than half that of GHF_α and less than one third that of GHF_{SR}. The range in difference values was largest for GHF_{SR}, more than three times the smallest values (M_{terr} and GHF_M). Linear artifacts were observed in the difference maps of GHF_{SR} and GHF_α, whereas the M_{terr} and GHF_M difference maps appeared to have no linear artifacts (Fig. 2).

M_{terr} and GHF_M values, in addition to having the same standard deviation (Tables 1, 2, and 3), were visually identical as a result of subtracting a constant for each year. The hottest M_{terr} and GHF_M pixels were found primarily in the 1988 fire scars and the Northern Range of YNP, while the coolest pixels appeared to be on north-facing slopes. The hottest GHF_{SR} pixels, on the other hand, were focused in the Northern Range and north-facing slopes, while the coolest pixels were on the south-facing slopes. The hottest GHF_α pixels were also located in the Northern Range and north-facing slopes, with more pixels visible in 1988 fire scars than GHF_{SR}, especially in 2002. The coolest GHF_α pixels were mostly on south-facing slopes and near Yellowstone Lake.

Table 3. Summary Statistics[a] for Differenced Images (2007 minus 2002) for Yellowstone National Park (Wm^{-2})

Equation	Min	Max	Mean	Median	Mode	Std. Dev.	Range
(2.8) M_{terr}	−81.9	71.0	−15.0	−15.0	−15.6	8.8	152.9
(2.9) GHF_M	−66.9	86.0	0.0	0.0	−0.6	8.8	152.9
(2.10) GHF_{SR}	−273.5	217.4	−15.1	−16.5	−14.6	14.0	490.9
(2.11) GHF_α	−253.8	186.5	−16.1	−16.4	−18.2	13.8	430.3

[a]Summary statistics: terrestrial emittance = M_{terr}; mean non-geothermal value corrected geothermal heat flux = GHF_M; potential annual direct incident solar radiation corrected geothermal heat flux = GHF_{SR}; and albedo and potential annual direct incident solar radiation corrected geothermal heat flux = GHF_α.

When the four methods discussed above (M_{terr}, GHF_M, GHF_{SR}, and GHF_α) were compared, the GHF_α method resulted in more of the hottest 10% of the pixels within the defined geothermal areas. The 60 × 60 m resolution GHF_α image collected in 2002 had 4,879 of the hottest pixels within the defined geothermal areas (21.7%), as compared to 1,452 pixels for GHF_{SR} (6.4%) and 3,949 pixels for GHF_M and M_{terr} (17.5%). The 120 × 120 m resolution GHF_α image collected in 2007 had 1,027 of the hottest pixels within the defined geothermal areas (19.4%), as compared to 255 pixels for GHF_{SR} (4.8%) and 678 pixels for GHF_M and M_{terr} (12.8%). The M_{terr} and GHF_M methods resulted in less of the coolest 10% of the pixels within the defined geothermal areas. The 60 × 60 m resolution M_{terr} and GHF_M images collected in 2002 had 333 of the coolest pixels within the defined geothermal areas (1.5%), as compared to 774 pixels for GHF_{SR} (3.4%) and 453 pixels for GHF_α (2.0%). The 120 × 120 m resolution M_{terr} and GHF_M images collected in 2007 had 42 of the coolest pixels within the defined geothermal areas (0.8%), as compared to 193 pixels for GHF_{SR} (3.6%) and 111 pixels for GHF_α (2.1%).

Over 12,000 individual geothermal features have been located by the Thermal Inventory Project. The hottest 10% of GHF_α pixels coincided with more of these Thermal Inventory Project points than did the hottest 10% of the M_{terr} pixels (Table 4). In 2002, the hottest 10% of GHF_α coincided with more than twice as many Thermal Inventory Project points as did the hottest 10% of M_{terr}. In 2007, the hottest 10% of GHF_α coincided with just under twice as many Thermal Inventory Project points as did the hottest 10% of M_{terr}.

The GHF_α method produced the largest difference when the mean values of pixels outside the defined geothermal areas were subtracted from the mean values of only the pixels within the defined geothermal areas (Tables 5 and 6), indicating more hot pixels within the defined geothermal areas with this method. The M_{terr} method had a larger difference than GHF_{SR}, but had less than half the difference of GHF_α.

Comparison to Airborne Data in the Norris Geyser Basin Area

The summary statistics of M_{terr} values were similar to the Hardy heat flow summary statistics (Table 7). The Hardy (2005) data had higher values overall than the M_{terr}
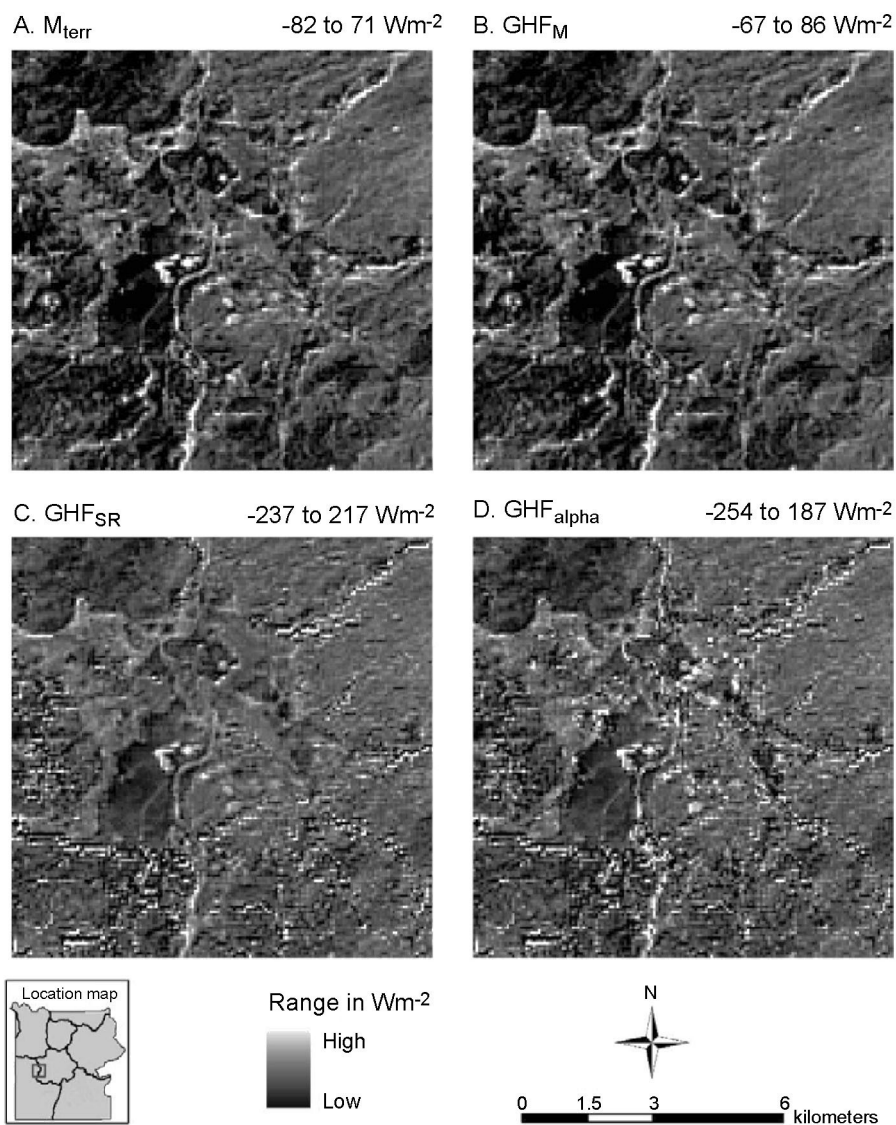
A. M$_{terr}$ -82 to 71 Wm^{-2} B. GHF$_M$ -67 to 86 Wm^{-2}

C. GHF$_{SR}$ -237 to 217 Wm^{-2} D. GHF$_{alpha}$ -254 to 187 Wm^{-2}

Location map

Range in Wm^{-2}
High
Low

N

0   1.5   3   6
kilometers

Fig. 2. Difference images (2007 minus 2002) of (A) terrestrial emittance (M$_{terr}$), (B) mean non-geothermal value corrected geothermal heat flux (GHF$_M$), (C) potential annual direct incident solar radiation corrected geothermal heat flux (GHF$_{SR}$), and (D) albedo and potential annual direct incident solar radiation corrected geothermal heat flux (GHF$_\alpha$) at Midway and Lower geyser basins in Yellowstone National Park (values are in Wm^{-2}).

data, with the maximum values much higher and the minimum values only slightly higher. The range of the Hardy data was more than double the range of the M$_{terr}$ data. The total heat flow values for M$_{terr}$ were within an order of magnitude of the Hardy heat flow data for both the full Hardy data extent and a subset that covers just Norris Geyser Basin (Table 8).

Table 4. Coincidence of Hottest 10% of M_{terr} and GHF_{α} with Thermal Inventory Project points in 2002 and 2007[a]

Method	Year	No. of coincident Thermal Inventory Project points
(2.8) M_{terr}	2002	1,661
(2.11) GHF_{α}	2002	3,642
(2.8) M_{terr}	2007	1,385
(2.11) GHF_{α}	2007	2,566

[a]M_{terr} = terrestrial emittance; GHF_{α} = albedo and potential annual direct incident solar radiation corrected geothermal heat flux

Table 5. July 5, 2002 Differences of Average Wm^{-2} Values Inside the Defined Geothermal Areas and Average Wm^{-2} Values Outside the Defined Geothermal Areas for M_{terr}, GHF_{SR}, and GHF_{α}[a]

Equation	Inside average	Outside average	Difference
(2.8) M_{terr}	377.3	368.8	8.5
(2.10) GHF_{SR}	92.4	88.6	3.9
(2.11) GHF_{α}	135.6	117.8	17.8

[a]M_{terr} = terrestrial emittance; GHF_{SR} = potential annual direct incident solar radiation corrected geothermal heat flux; GHF_{α} = albedo and potential annual direct incident solar radiation corrected geothermal heat flux.

DISCUSSION AND CONCLUSION

Incorporating estimated emissivity on a pixel-by-pixel basis rather than as an average over the entire image produced locally precise terrestrial emittance and GHF estimates by accounting for differences in emissivity due to varying amount of vegetation in each pixel. By deriving emissivity values from the finer-spatial-resolution reflective Landsat bands, more detail was incorporated into the M_{terr} values than if the thermal band had been used alone.

The M_{terr} values calculated for the July 2002 Landsat image were within the same order of magnitude of the heat flow values calculated by Hardy (2005) for the nighttime airborne October 2002 image of Norris Geyser Basin and surrounding area, providing some confirmation that the calculations used in this project were consistent with previous analysis. Solar radiation was not taken into account for either image. While there are fewer solar radiation effects during a nighttime image, there are still accumulated effects from the sun heating the ground the previous day, week, month, and year. The similarities between the daytime and nighttime readings are, therefore, expected, and show that Landsat can be used to calculate terrestrial emittance with comparable results to higher-spatial-resolution sensors.

Table 6. June 25, 2007 Differences of Average Wm^{-2} Values Inside the Defined Geothermal Areas and Average Wm^{-2} Values Outside the Defined Geothermal Areas for M_{terr}, GHF$_{SR}$, and GHF$_{\alpha}$ [a]

Equation	Inside average	Outside average	Difference
(2.8) M_{terr}	360.2	353.8	6.4
(2.10) GHF$_{SR}$	74.3	73.6	0.7
(2.11) GHF$_{\alpha}$	117.2	101.8	15.4

[a]M_{terr} = terrestrial emittance; GHF$_{SR}$ = potential annual direct incident solar radiation corrected geothermal heat flux; GHF$_{\alpha}$ = albedo and potential annual direct incident solar radiation corrected geothermal heat flux.

Table 7. Comparison of October 2002 Hardy (2005) Heat Data Summary Statistics to July 2002 Estimated Terrestrial Emittance (M_{terr}) Summary Statistics (values in Wm^{-2})[a]

	Min	Max	Mean	Median	Mode	Std. Dev.
Hardy full data extent						
Hardy data 60 m	342.2	664.3	407.7	401.3	387.5	35.7
M_{terr} 60 m	338.2	418.5	378.2	377.1	376.4	13.7
Norris Geyser Basin						
Hardy data 60 m	361.8	664.3	432.0	426.7	418.5	37.0
M_{terr} 60 m	353.4	418.5	387.5	387.7	393.3	11.9

[a]Information from the full 2002 Hardy data and Norris Geyser Basin extents are displayed.

The M_{terr} and Hardy heat flow values were larger for Norris Geyser Basin than for the larger extent, as expected. Reducing the study area to the smaller Norris Geyser Basin included less non-geothermal ground, and thus more heat would be emitted per area than in a larger, mostly non-geothermal-ground study area.

The M_{terr} and Hardy values were similar, but the differences are also noteworthy. Because the Landsat image was from July and solar radiation was not taken into account, M_{terr} values were expected to be greater than the Hardy heat flow values, but they were not. This is most likely due to the different data collection and processing methods. The Hardy data were derived directly from raw DNs and temperature calibration data. No atmospheric corrections were needed because the data were collected with a low-elevation airborne flight. The M_{terr} data, on the other hand, were not calibrated to ground temperature, and needed atmospheric corrections since they were collected from space.

Estimating terrestrial emittance requires only three Landsat bands and atmospheric and radiometric corrections. Terrestrial emittance includes all the types of heat emitted from the ground: GHF, direct incident solar radiation, and indirect solar

Table 8. Comparison of October 2002 Hardy (2005) Total Heat Flow and Power Values to July 2002 Estimated Terrestrial Emittance (M_{terr}) Heat Flow and Power Values[a]

	Hardy	M_{terr}	Area of analysis
Heat flow			
Hardy data extent	407.7 Wm^{-2}	378.2 Wm^{-2}	–
Norris Geyser Basin	432.0 Wm^{-2}	387.5 Wm^{-2}	–
Power			
Hardy data extent	7.0 GW	6.5 GW	17,125,200 m^2
Norris Geyser Basin	1.5 GW	1.4 GW	3,502,800 m^2

[a]All M_{terr} values are within an order of magnitude of the Hardy data.

effects, including convection from air currents and soil conduction of solar energy. Mean annual air temperature is a good representation of ground water temperature. Mean M_{terr} values were similar to, but slightly higher than, the average annual air temperature of YNP (Western Regional Climate Center, 2005), demonstrating that the model includes geothermal as well as non-geothermal heat. Many of the hottest M_{terr} pixels were located on low-elevation flat and south-facing slopes (in the Northern Range) and within 1988 fire scars that have been revegetated with thick stands of young lodgepole pine (*Pinus contorta*) intermixed with down and standing grey and white snags. The GHF$_M$ model simply subtracted one value across the image, therefore demonstrating the exact same spatial pattern as M_{terr} but with lower values. This model should have resulted in relatively fewer high values that represent only geothermal heat; however, due to the effects of direct and indirect solar radiation, GHF$_M$ was an inferior model for estimating true GHF. High values of GHF$_M$ were observed both in geothermal areas and on south-facing slopes with no geothermal activity, with many of the highest values not in the defined geothermal areas.

There are many parameters that must be included in a GHF calculation that are not readily available or straightforwardly modeled, including sensible and latent heat exchange with the atmosphere and advected heat flux in precipitation and runoff (Watson et al., 2008). Many of the direct solar radiation effects were modeled with the equation for SR (McCune and Keon, 2002). An estimation of GHF that included direct solar radiation was expected to remove many of the non-geothermal effects observed in M_{terr} and GHF$_M$. The method used to estimate GHF$_{SR}$ removed some, but not all, of the effects from direct solar radiation. The high M_{terr} and GHF$_M$ values from fire scars were reduced in the GHF$_{SR}$ model (white circles in Figs. 3C and 4C); however, the model overcompensated for solar and topographic effects on north-facing slopes, creating falsely warm regions (arrows in Figs. 3C and 4C). It also reduced the geothermal heat signal from within the defined geothermal areas (e.g., black circles in Figs. 3B and 3C and 4B and 4C, in the area of the Grand Prismatic Spring and Excelsior Geyser). The SR model represented annual direct incident solar radiation, and because the Landsat images used were acquired during the summer when solar elevation was high, the annual calculation overadjusted for north-facing slopes. This
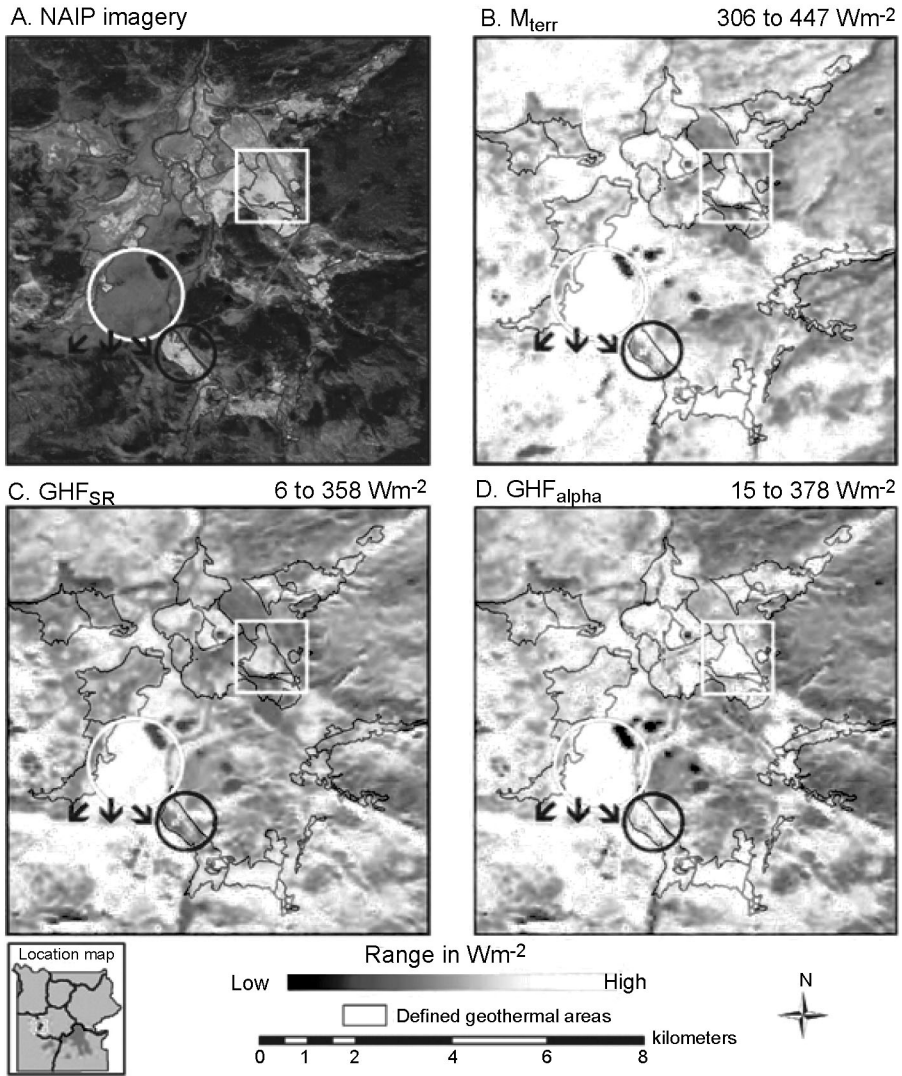
Fig. 3. A. National Agriculture Imagery Program (NAIP) imagery of Lower and Midway geyser basins, with Grand Prismatic Spring and Excelsior Geyser circled in black, a north-facing slope indicated by black arrows, a fire scar circled in white, and a geothermal barren shown in a white box. B. Terrestrial emittance (M_{terr}). C. Potential annual direct incident solar radiation corrected geothermal heat flux (GHF_{SR}). D. Albedo and potential annual direct incident solar radiation corrected geothermal heat flux (GHF_{α}) on July 5, 2002 (in Wm^{-2}).

model corrected a number of the solar radiation effects that were abundant in the M_{terr} model; however, it did not correct all solar radiation and albedo effects and overcorrected direct solar radiation in some locations. This model demonstrated potential for using Landsat data to estimate GHF.
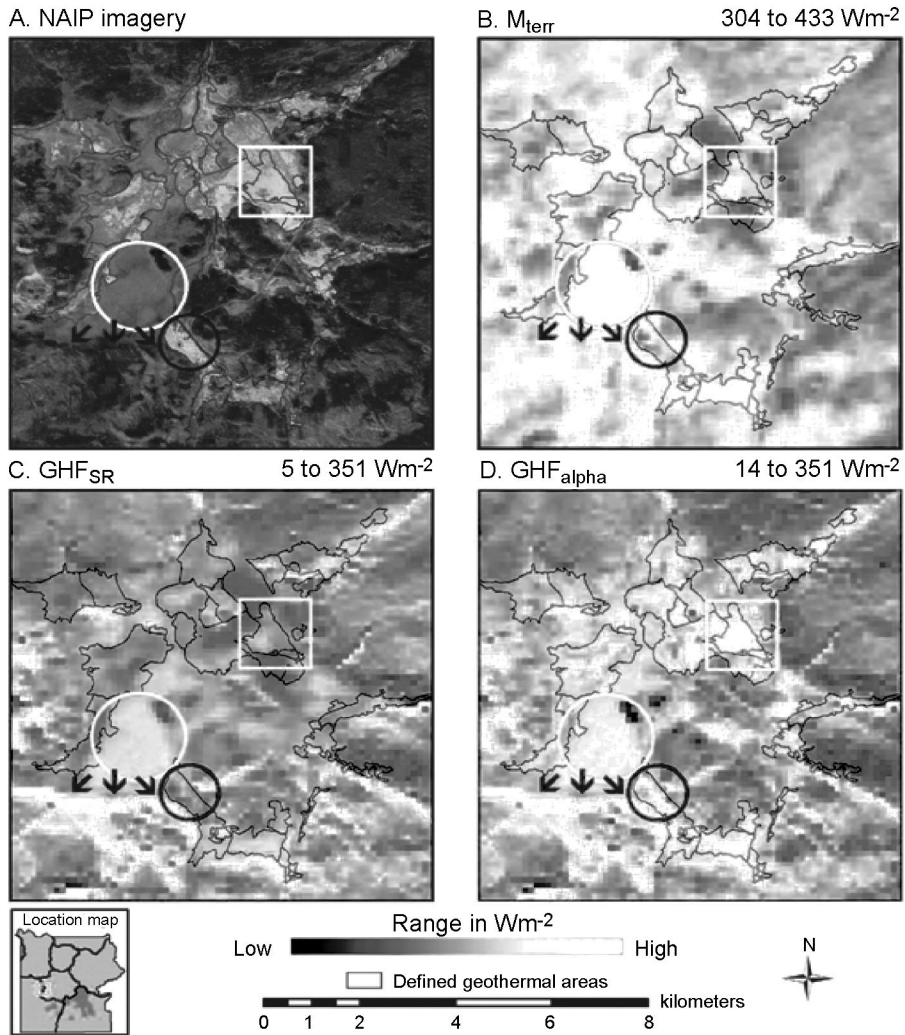
Fig. 4. A. National Agriculture Imagery Program (NAIP) imagery of Lower and Midway geyser basins, with Grand Prismatic Spring and Excelsior Geyser circled in black, a north-facing slope indicated by black arrows, a fire scar circled in white, and a geothermal barren shown in a white box. B. Terrestrial emittance (M_{terr}). C. Potential annual direct incident solar radiation corrected geothermal heat flux (GHF_{SR}). D. Albedo and potential annual direct incident solar radiation corrected geothermal heat flux (GHF_α) on June 25, 2007 (in Wm^{-2}).

Combining the effects of albedo with SR improved the GHF_{SR} model. More geothermal heat signatures were observed within the defined geothermal areas in the GHF_α model than in the GHF_{SR} model. Most of the geothermally active areas in YNP are white or grey surfaces with high albedos and low solar absorption. The equation for GHF_α appears to calculate the values for these active areas well (black circles in Figs 3D and 4D), but also possibly calculates values too high for white geothermal barrens

(white boxes in Figs. 3D and 4D). Most high values within fire scars were decreased in this model, although the north-facing slopes were still falsely warm (arrows in Figs. 3D and 4D). The GHF_α model shows promise, but without proper ground calibration it is uncertain to what extent it might be overcorrecting for direct solar and albedo effects. Indirect solar effects that are not included in this model must be accounted for as well.

When the four methods were compared, no one method was consistently superior. M_{terr} and GHF_α tended to produce more reasonable results than GHF_M and GHF_{SR}; however, the results from comparisons were inconclusive as to whether M_{terr} or GHF_α were more reasonable. GHF_α had more of the hottest 10% of the pixels within the defined geothermal areas, but M_{terr} had fewer of the coolest 10% of the pixels within the defined geothermal areas. All of the M_{terr} pixels had values higher than the average annual air temperature, but all of the GHF_α pixels had values lower than the average annual air temperature. The hottest 10% of GHF_α pixels coincided with approximately double the number of Thermal Inventory Project points than the hottest 10% of M_{terr} pixels. The difference in mean value inside the defined geothermal areas compared to the mean value outside the geothermal areas for GHF_α was more than double that of M_{terr}. Finally, the 2007 minus 2002 difference images indicated a very large range of change along with linear data artifacts in the GHF_α image, but a much smaller range of change and no linear data artifacts in the M_{terr} image.

This study established that estimation of absolute GHF with Landsat imagery is not possible without several additional parameters. Direct and indirect solar radiation and albedo remain as serious concerns and must be considered in future studies of this nature. Obtaining accurate absolute values of GHF with Landsat imagery—including the Landsat Data Continuity Mission that is expected to launch in December 2012 (NASA, 2010)—will require thermal ground calibration as well as methods of accounting for surface albedo and variations in solar radiation, both direct and indirect. Due to these unaccounted for effects, M_{terr} is unsatisfactory as a measure of absolute GHF. For change analysis within the defined geothermal areas, however, M_{terr} is likely the most appropriate thermal measure, even though the method comparisons were inconclusive. Albedo and solar radiation effects within the M_{terr} model tend to be relatively constant across the image over time, unless there has been a significant land cover change (e.g., from fire). Therefore, these effects are largely cancelled out for change analysis, with any differences between dates potentially related to changes in GHF. Utilizing M_{terr} for change analysis over recent decades is a prudent choice, because, in addition to the reasons outlined above, a version of M_{terr} has been field validated (Watson et al., 2008), it is the least-modified Landsat thermal data, it requires no field data collection (impossible for historic images), and it has no linear data artifacts.

ACKNOWLEDGMENTS

REFERENCES

Andres, R. J. and W. I. Rose, 1995, "Description of Thermal Anomalies on Two Active Guatemalan Volcanoes Using Landsat Thematic Mapper Imagery," *Photogrammetric Engineering & Remote Sensing*, 61(6):775–782.

Barsi, J. A, Hook, S. J., Schott, J. R., Raqueno, N. G., and B. L. Marham, 2007, "Landsat-5 Thematic Mapper Thermal Band Calibration Update," *IEEE Geoscience and Remote Sensing Letters*, 4(4):552–555.

Boomer, S. M., Lodge, D. P., Dutton, B. E., and B. Pierson, 2002, "Molecular Characterization of Novel Red Green Nonsulfur Bacteria from Five Distinct Hot Springs Communities in Yellowstone National Park," *Applied and Environmental Microbiology*, 68(1):346–355.

Bourgeois, O., Dauteuil, O., and B. Van Vliet-Lanoe, 2000, "Geothermal Control on Flow Patterns in the Last Glacial Maximum Ice Sheet of Iceland," *Earth Surface Processes and Landforms*, 25(1):59–76.

Brunsell, N. A. and R. R. Gillies, 2002, "Incorporating Surface Emissivity into a Thermal Atmospheric Correction," *Photogrammetric Engineering & Remote Sensing*, 68(12):1263–1269.

Carranza, E. J. M. and M. Hale, 2002, "Mineral Imaging with Landsat Thematic Mapper Data for Hydrothermal Alteration Mapping in Heavily Vegetated Terrane," *International Journal of Remote Sensing*, 23(22):4827–4852.

Chander, G., Markham, B. L., and D. L. Helder, 2009, "Summary of Current Radiometric Calibration Coefficients for Landsat MSS, TM, ETM+, and EO-1 ALI Sensors," *Remote Sensing of Environment*, 113(5):893–903.

Chavez, P. S., Jr., 1996, "Image-Based Atmospheric Corrections—Revisited and Revised," *Photogrammetric Engineering & Remote Sensing*, 62(9):1025–1036.

Coolbaugh, M. F., Kratt, C., Fallacaro, A., Calvin, W. M., and J. V. Taranik, 2007, "Detection of Geothermal Anomalies Using Advanced Spaceborne Thermal Emission and Reflection Radiometer (ASTER) Thermal Infrared Images at Bradys Hot Springs, Nevada, USA," *Remote Sensing of Environment*, 106(3):350–359.

Custer, S. G., Michels, D. E., Sill, W., Sonderegger, J. L., Weight, W., and W. Woessner, 1993, *Recommended Boundary for Controlled Groundwater Area in Montana Near Yellowstone Park*, Fort Collins, CO: U.S. Department of the Interior National Park Service.

Daneshfar, B., Desrochers, A., and P. Budkewitsch, 2006, "Mineral-Potential Mapping for MVT Deposits with Limited Data Sets Using Landsat Data and Geological Evidence in the Borden Basin, Northern Baffin Island, Nanuvut, Canada," *Natural Resources Research*, 15(3):129–149.

Dogan, H. M., 2008, "Applications of Remote Sensing and Geographic Information Systems to Assess Ferrous Minerals and Iron Oxide of Tokat Province in Turkey," *International Journal of Remote Sensing*, 29(1):221–233.

Elachi, C., 1987, *Introduction to the Physics and Techniques of Remote Sensing,* New York, NY: John Wiley & Sons, 413 pp.

Flynn, L. P., Harris, A. J. L., and R. Wright, 2001, "Improved Identification of Volcanic Features Using Landsat 7 ETM+," *Remote Sensing of Environment*, 78(1–2):180–193.

Fournier, R. O., White, D. E., and A. H. Truesdell, 1975, "Convective Heat Flow in

Yellowstone National Park," in *Proceedings of the Second United Nations Symposium on the Development and Use of Geothermal Resources*, 731–739.

Friedman, I. and D. R. Norton, 2007, "Is Yellowstone Losing Its Steam?—Chloride Flux out of Yellowstone National Park," in *U.S. Geological Survey Professional Paper 1717*, 272–297.

Gruber, S., Hoelzle, M., and W. Haeberli, 2004, "Rock-Wall Temperatures in the Alps: Modeling Their Topographic Distribution and Regional Differences," *Permafrost and Periglacial Processes*, 15(3):299–307.

Hardy, C. C., 2005, *Characterizing Thermal Features from Multi-spectral Remote Sensing Data Using Dynamic Calibration Procedures*, Missoula, MT: University of Montana, 153 pp.

Heasler, H., Jaworowski, C., and D. Susong, 2004, *A Geothermal Monitoring Plan for Yellowstone National Park*, Yellowstone National Park, WY: Yellowstone Center for Resources, 24 pp.

Kaneko, T. and M. J. Wooster, 1999, "Landsat Infrared Analysis of Fumarole Activity at Unzen Volcano: Time-Series Comparison with Gas and Magma Fluxes," *Journal of Volcanology and Geothermal Research*, 89(1–4):57–64.

Kohl, T., 1999, "Transient Thermal Effects below Complex Topographies," *Tectonophysics*, 306(3–4):311–324.

Liang, S., 2000, "Narrowband to Broadband Conversions of Land Surface Albedo: I Algorithms," *Remote Sensing of Environment*, 76(2):213–238.

McCune, B. and D. Keon, 2002, "Equations for Potential Annual Direct Incident Radiation and Heat Load," *Journal of Vegetation Science*, 13(4):603–606.

MontanaView, 2008, "MontanaView Supporting Remote Sensing" [http://montana view.org/], last accessed on April 8, 2009.

NASA, 2008, "ASTER Spectral Library" [http://speclib.jpl.nasa.gov/], last accessed on March 3, 2009.

NASA, 2009, "Landsat 7 Science Data Users Handbook" [http://landsathandbook. gsfc.nasa.gov/handbook.html], last accessed on April 6, 2009.

NASA, 2010, "Landsat Data Continuity Mission" [http://ldcm.gsfc.nasa.gov/mission_ details.html], last accessed October 15, 2010.

Norton, D. R. and I. Friedman, 1985, "Chloride Flux out of Yellowstone National Park," *Journal of Volcanology and Geothermal Research*, 26(3–4):231–250.

Ontar Corporation, 2001, *PcModWin 4.0 Ver 1.01: User Interface Environmnet for MODTRAN 4.0*, North Andover, MA: Ontar Corporation [www.ontar.com], last accessed on June 29, 2009.

Parmenter, A. W., Hansen, A., Kennedy, R. E., Cohen, W., Langner, U., Lawrence, R., Maxwell, B., Gallant, A., and R. Aspinall, 2003, "Land Use and Land Cover Change in the Greater Yellowstone Ecosystem: 1975–1995," *Ecological Applications*, 13(3):687–703.

Patrick, M., Dean, K., and J. Dehn, 2004, "Active Mud Volcanism Observed with Landsat 7 ETM+," *Journal of Volcanology and Geothermal Research*, 131(3–4):307–320.

Seielstad, C., and L. Queen, 2009, *Thermal Remote Monitoring of the Norris Geyser Basin, Yellowstone National Park*, Final Report for the National Park Service Cooperative Ecosystem Studies Unit, Agreement No. H1200040001, 38 pp.

Shaw, J.A. and C. Marston, 2000, "Polarized infrared emissivity for a rough water

surface," *Optics Express*, 7(11):375–380.

Smith, R. B. and L. J. Siegel, 2000, *Windows Into the Earth—The Geologic Story of Yellowstone and Grand Teton National Parks*, New York, NY: Oxford University Press, 242 pp.

Song, Y., Kim, H.-C., Yum, B.-W., and E. Ahn, 2005, "Direct-Use Geothermal Development in Korea: Country Update 2000–2004," in *Proceedings of the World Geothermal Congress*, 1–7.

Sorey, M. L., 1991, *Effects of Potential Geothermal Development in the Corwin Springs Known Geothermal Resources Area, Montana, on the Thermal Features of Yellowstone National Park*, Menlo Park, CA: U.S. Geological Survey, Water-Resources Investigations Report 91-4052, 204 pp.

Spatial Analysis Center, 1998, *30-Meter Elevation Data for Yellowstone National Park, Wyoming, Montana, Idaho*, Yellowstone National Park, WY: Yellowstone Center for Resources (digital spatial data).

Spatial Analysis Center, 2000, *Precipitation in Yellowstone National Park, Wyoming, Montana, Idaho*, Yellowstone National Park, WY: Yellowstone Center for Resources (digital spatial data).

Spatial Analysis Center, 2005, *Hydrogeothermal Areas of Yellowstone National Park, Wyoming, Montana, Idaho*, Yellowstone National Park, WY: Yellowstone Center for Resources (digital spatial data).

Urai, M., 2002, "Heat Discharge Estimation Using Satellite Remote Sensing Data on the Iwodake Volcano in Satsuma-Iwojima, Japan," *Earth, Planets, Space*, 54(3):211–216.

Utah State University, 2008, "Image Standardization: At-Sensor Reflectance and COST Correction" [http://earth.gis.usu.edu/imagestd/], last accessed on April 8, 2009.

Waite, G. P., and R. B. Smith, 2002, "Seismic Evidence for Fluid Migration Accompanying Subsidence of the Yellowstone Caldera," *Journal of Geophysical Research*, 107(B9, 2177): ESE 1-1–ESE 1-15.

Watson, F. G. R., Lockwood, R. E., Newman, W. B., Anderson, T. N., and R. A. Garrott, 2008, "Development and Comparison of Landsat Radiometric and Snow-pack Model Inversion Techniques for Estimating Geothermal Heat Flux," *Remote Sensing of Environment*, 112(2):471–481.

Watson, K., 1975, "Geologic Applications of Thermal Infrared Images," *Proceedings of the IEEE*, 63(1):128–137.

Western Regional Climate Center, 2005, "Period of Record Monthly Climate Summary—Yellowstone Park, Wyoming (489905)" [http://www.wrcc.dri.edu/cgi-bin/cliRECtM.pl?wyyell], last accessed on April 6, 2009.